metals

MDPI

Article

Effect of Electromagnetic Field Assistance on the Wear and Corrosion Resistance of Nickel-Based Coating by Laser Cladding

Dianxian Zhan [1], Dezhi Jiang [2], Yonggang Tong [1], Mingjun Zhang [1], Jian Zhang [1], Hongwei Hu [1], Zhenlin Zhang [3,*] and Kaiming Wang [1,*]

[1] College of Automotive and Mechanical Engineering, Changsha University of Science and Technology, Changsha 410114, China
[2] School of Materials Science and Engineering, Zhengzhou University of Aeronautics, Zhengzhou 450046, China
[3] School of Materials Science and Engineering, Southwest Jiaotong University, Chengdu 610031, China
* Correspondence: zzl21@swjtu.edu.cn (Z.Z.); kmwang@csust.edu.cn (K.W.)

Abstract: Offshore wind turbine generators usually demand higher requirements for key component materials because of the adverse working environment. Therefore, in this study, electromagnetic-assisted laser cladding technology was introduced to prepare the nickel-based composite coating on the Q345R matrix of wind turbine generator key component material. By means of Scanning Electron Microscope (SEM), X-ray diffraction (XRD), Energy Dispersive Spectrometer (EDS), the Vickers hardness tester, friction and wear tester, and electrochemical workstation, the effects of different magnetic field intensities on the macroscopic morphology, microstructure, phase composition, microhardness, wear resistance, and corrosion resistance of the coating were analyzed. The experimental results show that the addition of a magnetic field can effectively reduce the surface defects, improve the surface morphology, and not change the phase composition of the coating. With the increase in magnetic field intensity, the microstructure is gradually refined, and the average microhardness increases gradually, reaching a maximum of 944$HV_{0.5}$ at 8 T. The wear resistance gradually increases with the increase in magnetic field intensity, especially when the magnetic field intensity reaches 12 T, the wear rate of the coating is reduced by 81.13%, and the corrosion current density is reduced by 43.7% compared with the coating without a magnetic field. The addition of an electromagnetic field can enhance the wear resistance and corrosion resistance of the nickel-based laser cladding layer.

Keywords: laser cladding; steady magnetic field; nickel-based coating; microstructure; wear resistance; corrosion resistance

Citation: Zhan, D.; Jiang, D.; Tong, Y.; Zhang, M.; Zhang, J.; Hu, H.; Zhang, Z.; Wang, K. Effect of Electromagnetic Field Assistance on the Wear and Corrosion Resistance of Nickel-Based Coating by Laser Cladding. *Metals* **2024**, *14*, 998. https://doi.org/10.3390/met14090998

Academic Editor: Mosab Kaseem

Received: 27 July 2024
Revised: 29 August 2024
Accepted: 30 August 2024
Published: 1 September 2024

1. Introduction

The generator is one of the key components in wind power; its function is to convert the wind energy captured by the impeller into electric energy. In so doing, the bearing position of the generator's key components is prone to wear. After wear, the generator vibrates, which results in a large amount of energy being converted into heat and noise, which adversely affects the generation and stable operation of the fan. In addition, the offshore wind turbine generator's key components work in a high salt environment for a long time, which also demands higher requirements for the corrosion resistance of the key components. Key component failure caused by wear and corrosion exacerbates the power generation loss of wind turbines, and the repair and replacement cost is high, which adds huge pressure to the operation of wind farms [1–4]. Therefore, the preparation of a high-performance coating on the key component surfaces is a better choice to improve the wear resistance and corrosion resistance of the generator's key components.

Laser cladding is an advanced surface treatment technology that uses a high-energy laser as a heat source to deposit coatings on the surface of a substrate. Generally, the prepared coatings have a low dilution rate and high corrosion and wear resistance, so are

widely used in the manufacture and repair of key parts in the automotive, metallurgy, oil and gas, aerospace, and other fields [5–8]. Due to the high solidification rate and large temperature gradient, traditional laser cladding technology usually faces problems such as cracks and pores, which result in a decline in the surface quality performance of the coating [9]. Therefore, many scholars adopt the method of applying an external field to improve these problems. For example, Wang et al. [10] studied the influence of the direction and size of current assisted by an electromagnetic field on the coating structure and segregation. The results showed that the segregation phenomenon decreased first and then increased with the increase in current, and the hardness increased first and then decreased. Zhai et al. [9] used electromagnetic field assistance to clad nickel-based coatings on a pure iron surface and obtained external auxiliary field parameters under the optimal value of molten pool temperature. The parameters were a magnetic field intensity of 0.2 T and an alternating current (AC) of 1200 A. Wang et al. [11] concluded that a steady-state magnetic field can reduce the coating cracks and increase the hardness through the magnetic field-assisted laser cladding of nickel-based alloys. Therefore, the magnetic field can have a positive effect on the microstructure and properties of the laser cladding layer.

Nickel-based alloy coating is often used as the raw material for surface coating of parts in wear-resistant and corrosion-resistant environments because of its good wear resistance and fatigue resistance [12–14]. However, the conventional laser cladding technology is prone to cracking and other phenomena in nickel-based coatings. Q345R steel belongs to the low-alloy steel category, which has excellent welding performance, high strength and toughness, and low cost. It is widely used in the manufacturing of key components in wind power. However, the working environment of key components in wind power is harsh, and wear and corrosion may occur after a period of use. Improving the surface properties of Q345R steel is crucial for extending the lifespan of key components in wind power. Therefore, in order to further reduce the defects of the cladding layer and enhance the microstructure and properties of the nickel-based composite cladding layer, a nickel-based alloy coating was prepared on a Q345R steel plate by electromagnetic field-assisted laser cladding technology in this study, and the changes in the surface morphology, microstructure, phase, hardness, wear resistance, and corrosion resistance of the cladding layer with different magnetic fields were studied. The research results can provide theoretical guidance and technical support for the manufacture and repair of offshore wind power key components.

2. Materials and Methods

In the experiment, a Q345R steel plate of 100 mm × 70 mm × 15 mm was used as the substrate material, and the chemical composition is shown in Table 1. The cladding material was a nickel-based alloy powder with a particle size of 55~105 μm, whose chemical composition is shown in Table 2. The coated powder was placed in a drying oven and dried at 120 °C for 1 h to remove moisture and improve fluidity.

Table 1. Chemical composition of Q345R alloy steel (wt.%).

C	Si	Mn	P	S	Cu	Ni	Cr	Nb
≤0.20	≤0.55	1.20–1.70	≤0.025	≤0.010	≤0.30	≤0.30	≤0.30	≤0.050

Table 2. Chemical composition of the nickel-based powder (wt.%).

Si	Mo	Cr	B	C	Fe	Cu	Mo	Ni
4.0	3.0	15.5	3.0	0.75	14.0	2.5	2.5	Bal.

The laser cladding system is a 6 KW fiber laser combined with electromagnetic generators with different magnetic field intensities. In order to further study the effect of magnetic field intensity on the properties of laser cladding nickel-based coatings, four

different magnetic field intensities of 0 T, 4 T, 8 T, and 12 T were set in this study, and the samples prepared under these different magnetic fields were compared. Based on the previous experiments, the laser process parameters were optimized: the laser power was 2000 W, scanning speed was 240 mm/min, spot diameter was 3 mm, powder feed rate was 12 g/min, and argon flow rate was 9 L/min. Therefore, the cladding was carried out directly at the magnetic field intensity of 0 T, 4 T, 8 T, and 12 T through the optimal process parameters. After the cladding was finished, the cladding sample was cut into 20 mm × 10 mm × 10 mm metallographic samples by an electric spark wire cutting machine, and the surface of the sample was ground with 320-mesh~2000-mesh sandpaper, in turn. The polishing liquid was 2.5 μm diamond polishing liquid. After polishing, the sample was blow-dried and then corroded with aqua regia corrosion solution.

The microstructure was analyzed by scanning electron microscopy. The phase of the laser cladding layer was calibrated and analyzed by X-ray diffraction with the following parameters: Cu-kα radiation, voltage of 40 kV, current of 40 mA, scanning angle of 20° to 80°, and scanning step of 0.02°. The hardness test was carried out by a Vickers hardness tester (HVST-1000Z), the load was 5 N, the loading time was 10 s, and the average value was measured 5 times at each position. A friction and wear testing machine (HT-1000) was used to test the wear resistance at room temperature. The grinding material was a Si_3N_4 ceramic ball, the load was 10 N, the motor speed was set to 500 r/min, and the friction radius was controlled at 3 mm. Before the test began, the surface of the cladding was treated using a grinder and sandpaper (400–2000 mesh). The surface roughness of the wear test specimens was consistent. The experiment was carried out at room temperature (25 °C) for 30 min. After the wear test, the wear surface was observed through a VKX200 laser confocal microscope to evaluate the friction and wear properties of the coating.

Finally, an electrochemical workstation (CHI760E) was used to test the corrosion resistance with a 3.5% NaCl solution. The working electrode was the sample, the reference electrode was saturated calomel, and the auxiliary electrical level was platinum. To bring the sample to a steady state in solution, an open circuit potential (OCP) test was performed for 60 min before the AC impedance (EIS) measurement. The AC impedance test used an AC amplitude of 10 mV and a test frequency range of 10^5 to 10^{-2} Hz. Finally, a potentiodynamic polarization test (PD) was carried out with a scanning rate of 1 mV/s and a test range of −1 V~1.5 V.

3. Results and Discussion

3.1. Effect of an Electromagnetic Intensity on the Macromorphology of the Cladding Layer

Figure 1 shows the cross-section morphology of the coatings prepared under different magnetic field intensities. It is found that without a magnetic field, the bonding strength of the coating is low, and the coating cracks are obvious. With an increase in magnetic field intensity, the cracks gradually decrease. No obvious cracks appear at a high magnetic field intensity. This is because with the assistance of the magnetic field, the mass and heat transfer of the molten pool is strengthened, and the temperature gradient is reduced, so the cladding layer is cooled and solidified uniformly, the pores escape from the molten pool upward [15], and the residual stress generated during the cladding process is reduced, thus reducing the occurrence of cracks [16]. It can be seen from the figure that the width of the coating gradually increases under the action of a stable magnetic field compared with no magnetic field, from 4.02 mm under 0 T to 4.25 mm under 12 T, and the dilution rate and aspect ratio also show increasing trends. With an increase in magnetic field intensity, the effect is more obvious.

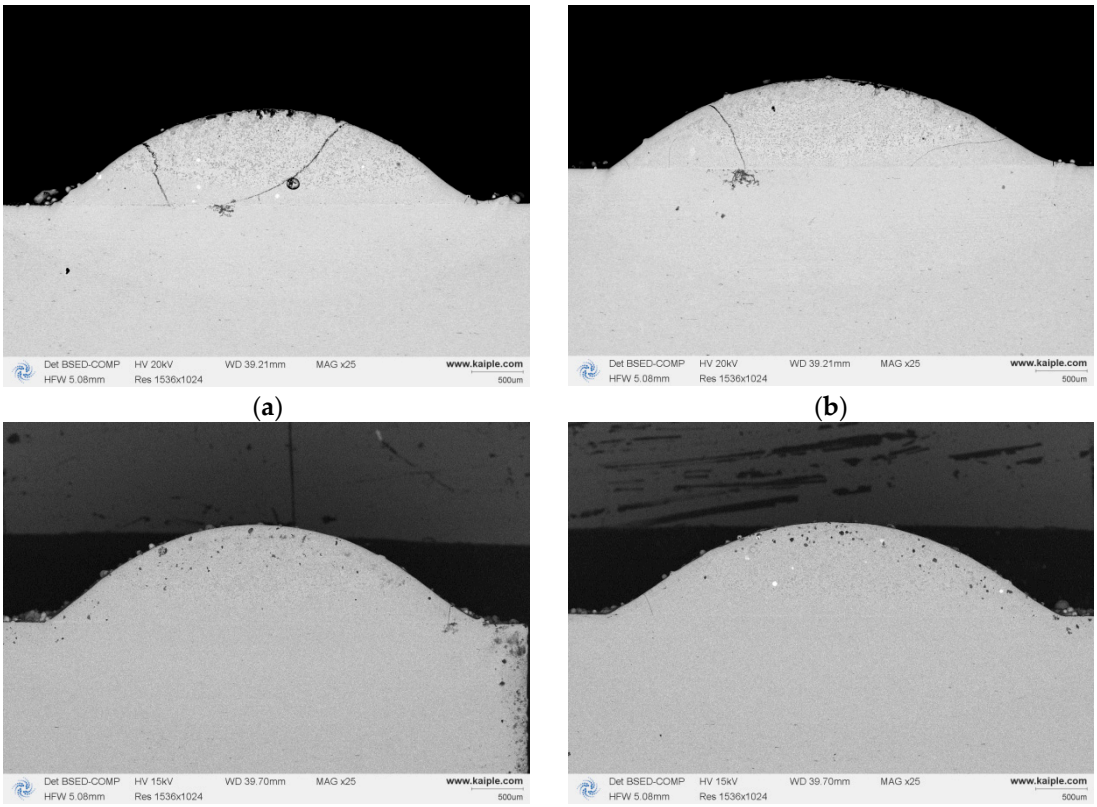

Figure 1. Cross-sectional morphologies of the coatings under different magnetic field intensities: (**a**) 0 T; (**b**) 4 T; (**c**) 8 T; (**d**) 12 T.

3.2. Effect of Electromagnetic Intensity on the Phase Composition of the Cladding Layer

The phase composition of the cladding layer prepared under different magnetic fields is shown in Figure 2. It can be seen in Figure 2 that the four cladding layers all produce diffraction peaks at the same position, and the main phases in the coating are γ-Ni, M_7C_3, M_2B (M: Cr, Fe), CrB, and Ni_3B. The external stable magnetic field does not change the phase composition of the coating. It can be seen in Figure 2a that the grain size of the cladding layer decreases after the magnetic field is added, according to the Debye–Scherrer formula [17]. Compared with the diffraction peak of the cladding layer prepared at 0 T, the diffraction peaks of the cladding layers prepared at 4 T, 8 T, and 12 T are slightly left offset. The amplified diffraction peaks of γ-Ni on the (111), (002), and (022) crystal planes are shown in Figure 2b–d [18]. With the increase in magnetic field intensity, the peak position of γ-Ni on these three crystal planes moves to a lower angle. This is because after the addition of magnetic field assistance, the internal temperature gradient of the cladding layer decreases, and the thermal stress of the cladding layer changes greatly, which results in different degrees of lattice distortion inside the four cladding layers [9,19]. That is to say, the lattice constant of the γ-Ni solid solution matrix changes. The γ-Ni solid solution has a face-centered cubic structure; the expression of lattice spacing in the cubic crystal system is mentioned in the reference [11], and the expression of lattice constant can be obtained from Bragg equation $2d\sin\theta = n\lambda$ [20]. The particle size is calculated by the Debye–Scherrer formula. According to the calculated results, the lattice constant increases, and the grain size decreases with the increase in magnetic field intensity.

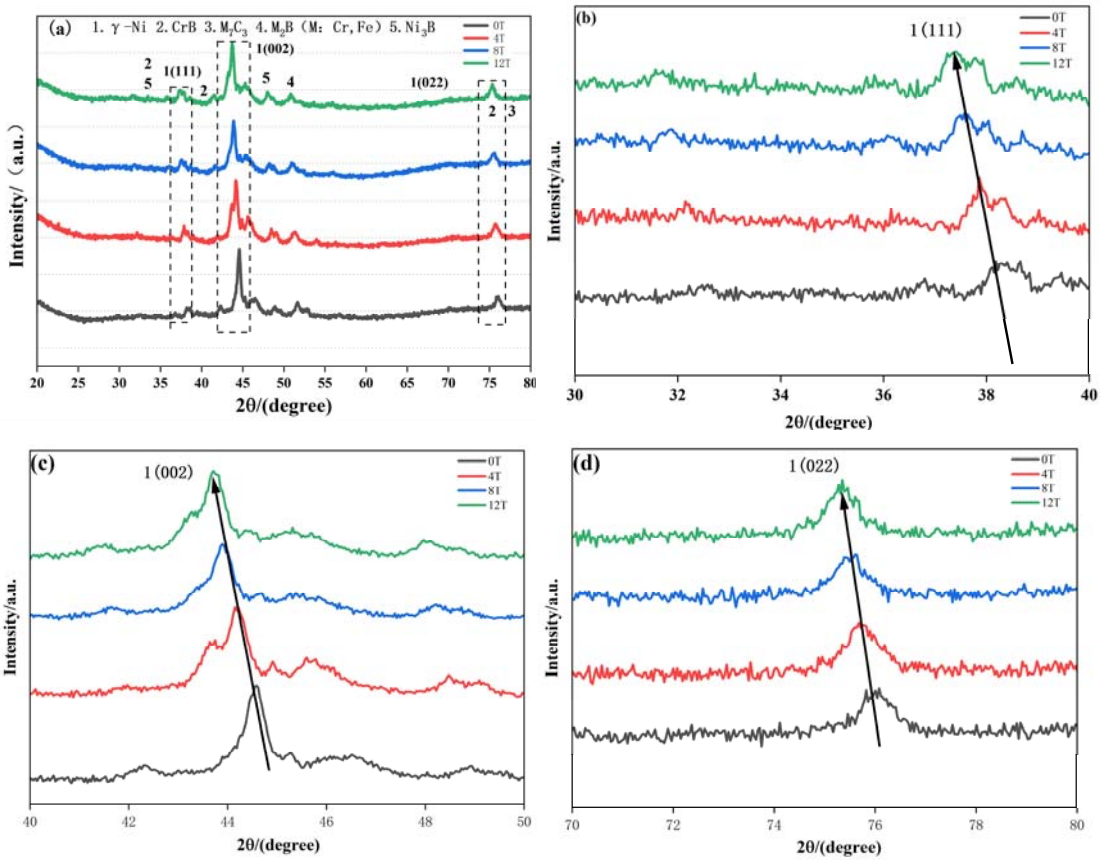

Figure 2. XRD of the coating at different magnetic field intensities: (**a**) 2θ = 20°~80°; (**b**) 2θ = 30°~40°; (**c**) 2θ = 40°~50°; (**d**) 2θ = 70°~80°.

3.3. Effect of an Electromagnetic Intensity on the Microstructure

The microstructure of the cladding layer is shown in Figure 3. It can be seen in Figure 3 that the microstructure of the cladding layer under different magnetic field intensities is similar, mainly composed of the matrix structure of gray A, the precipitated phase of massive B, the precipitated phase of strip C, and the eutectic structure of grayish-white D. The microstructure of gray phase A is equiaxed. Combined with the XRD results in Figure 2a, it is inferred to be γ-Ni by reference to the high Ni content in place A shown in Table 3. The black massive phase B is rich in Cr and B elements, and, combined with the position of the diffraction peak in Figure 2, it is inferred that it is hard phase CrB. The strip precipitated phase C is rich in Cr, and the contents of Fe and B elements do not decrease significantly in these regions; the grayish-white phase D is distributed near the nickel base matrix. Combined with the position of the diffraction peak in Figure 2, it can be inferred that it is CrFeB and Ni-B-Si eutectic, with reference to the EDS content results in Table 3. In addition, the gray phase A is solidly dissolved by Fe and other elements. As can be seen from the content of the Fe element at A in Table 3, the matrix phase A is also often referred to as a γ- (Ni, Fe) matrix. It can be seen from Figure 3a that without the assistance of a magnetic field, the massive hard phase of CrB is large and dispersed, and the strip phase C has a large size. The grain sizes of the massive phase B and strip phase C are significantly refined [20,21], and the eutectic phase D also gradually increases when a steady magnetic field is added. As can be seen from Figure 3c, the addition of a magnetic field causes some hard phase CrB grains to begin to distribute in clusters. With the increase in magnetic field intensity, the cluster phenomenon becomes more obvious and gradually shifts toward the steady magnetic field, resulting in segregation. This is because the electromagnetic braking effect reduces the speed of convection, resulting in a serious segregation of tissues. In

addition, the electromagnetic damping phenomenon causes the deflection of ferromagnetic CrB under the influence of electromagnetic force [22].

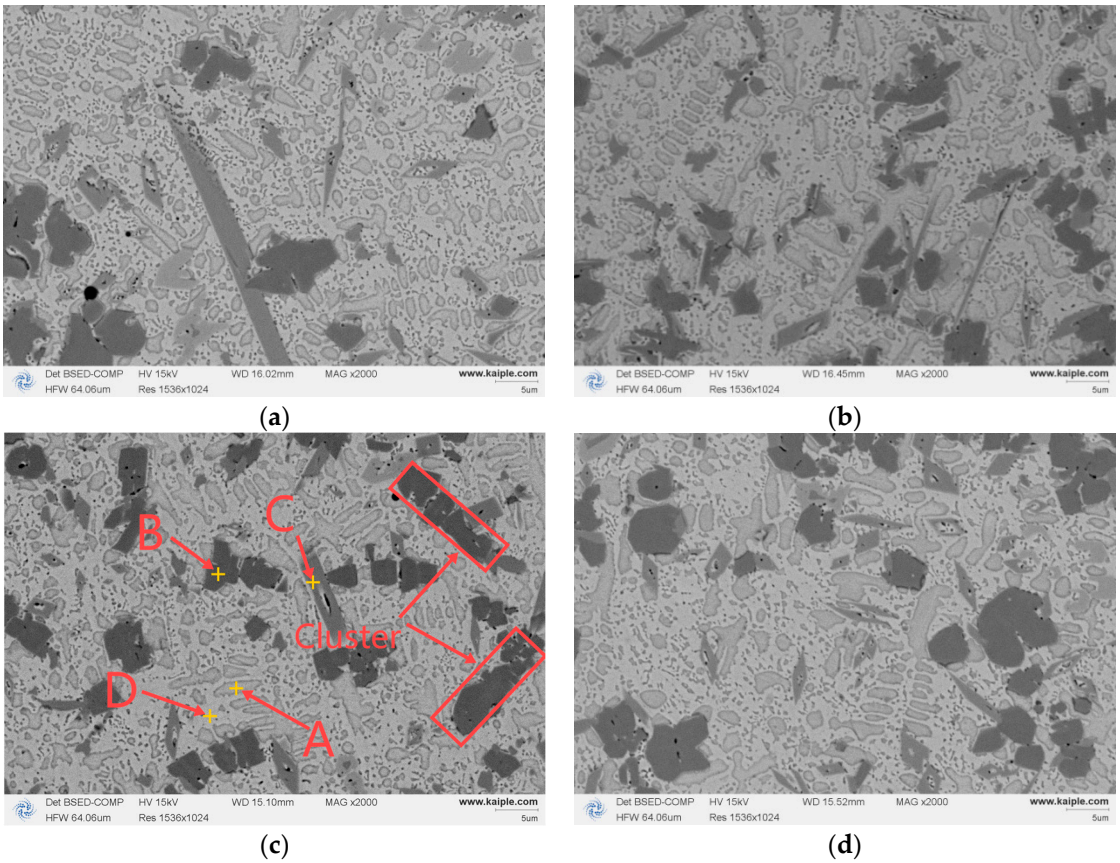

Figure 3. Microstructure of the middle–upper parts of the cladding layer under different magnetic field intensities: (**a**) 0 T; (**b**) 4 T; (**c**) 8 T; (**d**) 12 T.

Table 3. EDS point of the cladding layer (wt.%).

Spot Scanning Position	Element/Mass Fraction wt.%					
	Cr	B	C	Si	Fe	Ni
A	4.00	3.89	9.02	3.11	15.67	Bal.
B	62.01	12.44	8.26	0.24	4.38	Bal.
C	45.28	2.72	10.98	0.88	6.86	Bal.
D	13.98	1.35	9.65	1.45	12.35	Bal.

Figure 4 shows the mapping results of some elements in the middle–upper parts of the cladding layer at 0 T and 12 T. In order to observe the segregation phenomenon of hard phase CrB more obviously, the Ni, Cr, and B elements in the two coatings were analyzed. It can be seen from the figure that the addition of the magnetic field leads to a more uneven distribution of Cr and B elements, which enhances the segregation phenomenon of the Cr and B elements. The results are similar to those of the microstructure observation.

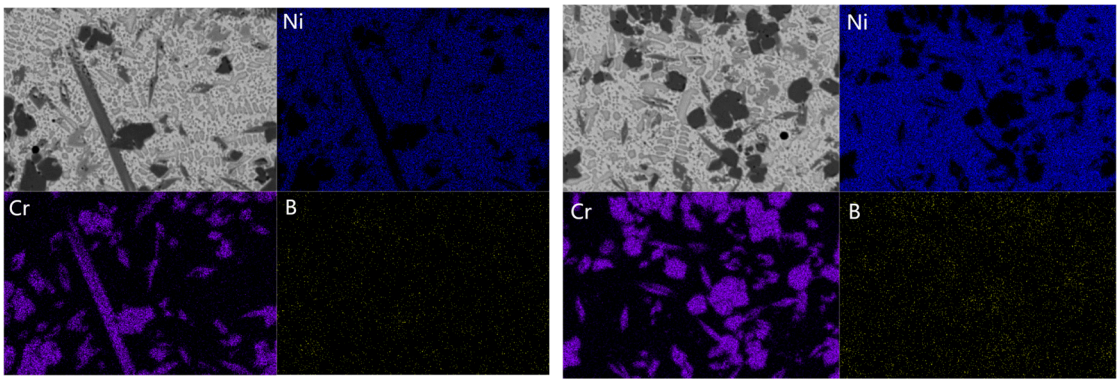

Figure 4. EDS mapping results of the middle–upper parts of the cladding layer: (**a**) EDS mapping results at 0 T; (**b**) EDS mapping results at 12 T.

3.4. Effect of an Electromagnetic Intensity on the Microhardness

The average hardness of the four cladding layers is shown in Figure 5. It can be seen from the hardness results that the hardness of the coating increases with the increase in the magnetic field intensity. The hardness reaches the maximum at 8 T with an average hardness of 944 $HV_{0.5}$, but when the magnetic field intensity reaches 12 T, the hardness decreases to 874 $HV_{0.5}$, which is below the hardness at 0 T of 908 $HV_{0.5}$ and 4 T of 910 $HV_{0.5}$. It can be concluded that within a certain range of magnetic field intensity, the coating hardness increases with the increase in magnetic field intensity, and the change in microhardness is closely related to the microstructure of the coating [23]. The microhardness of hard phase CrB is approximately 2185 ± 235 HV [24]; the increase in microhardness is promoted by the grain refinement and cluster aggregation of hard phase CrB [25,26]. In addition, with the increase in magnetic field intensity, the decrease in coating cracks also contributes to the increase in the microhardness of the cladding layer [27].

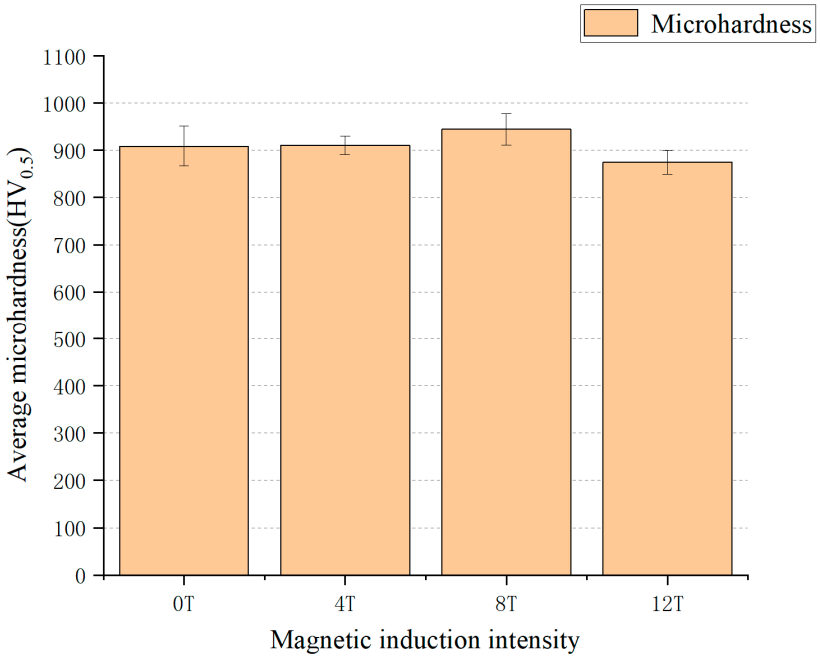

Figure 5. Average hardness of the cladding layer under different magnetic field intensities.

3.5. Effect of an Electromagnetic Intensity on the Wear Resistance

Figure 6 shows the coefficient of friction (COF) of the nickel-based coating under different magnetic field intensities. As can be seen from the COF curve, the wear process

can be divided into two typical stages: (1) the rapid rise stage; and (2) the stable wear stage [28]. It can be seen in the figure that the average COF of the coating prepared at 0 T is the largest at 0.31, and the COF gradually decreases with the increase in the magnetic field intensity. In the rapid rise stage, the COF is very small because the surface of the sample is smooth, the Si_3N_4 grinding ball is in point contact with the surface, and the stress is large. With the progress of the friction, the grinding ball is subjected to very large resistance. At this time, the COF rapidly rises to the maximum value of the entire wear stage, with violent fluctuations. When the friction and wear process is carried out for about 5 min, the contact mode changes from point contact to surface contact, and the friction and wear enter the stable stage, at which time the COF is relatively stable. First, the grinding ball will cut the softer material to form a scratch, and the grinding ball will further remove the sample material as the friction loss process progresses. As can be seen from the figure, the average COF of the coating at 12 T is 0.29, which is 6.5% lower than that of the coating at 0 T. Combined with Figure 3a, it can be seen that the size of the γ-Ni matrix phase and CrB are relatively large in the coating prepared without a stable magnetic field. When the stable magnetic field is applied, the grain size of the γ-Ni matrix and hard phase CrB is refined, and some CrB grains are distributed in clusters, which improves the hardness of the coating. In addition, during the wear process, the hard phase of these clusters is broken under the grinding ball pressure to form grinding chips, resulting in an anti-wear effect and thus reducing the COF of the coating [3]. During wear, the oxide film on the surface of the coating is continuously produced and removed to lubricate the surface. It can also be seen in Figures 3 and 5 that surface grain refinement increases the hardness of the coating, decreases the plastic deformation, and increases the wear resistance [29].

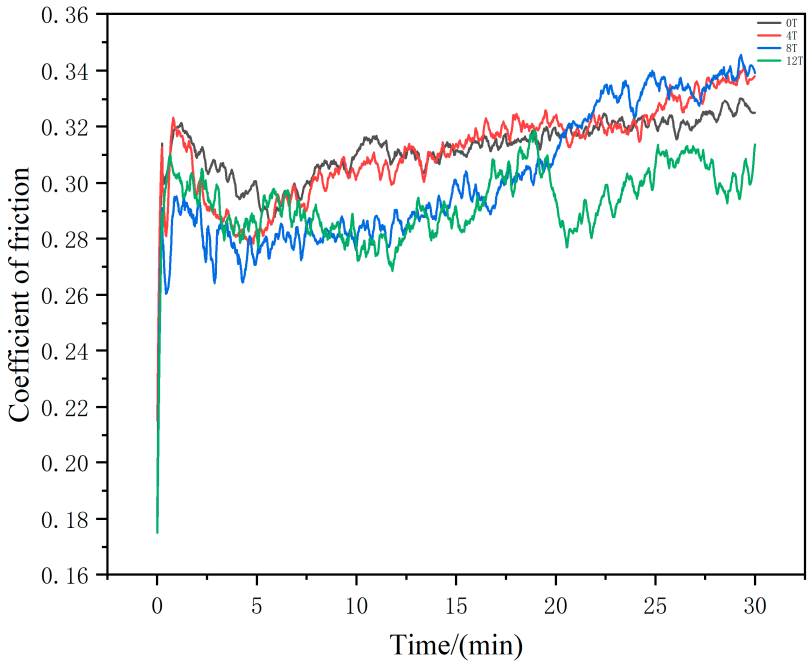

Figure 6. COF of the cladding layer under different stable magnetic field intensities (25 °C).

In order to better evaluate the friction and wear properties of the coating under different magnetic field intensities, the wear mark width of the sample was observed and measured, and the results are shown in Figure 7. The wear-width values of all the samples were measured by scanning electron microscopy. In order to ensure the accuracy of the data, each sample was measured three times to take the average value. As shown in the figure, the measured average widths of the wear marks are 343 μm, 240 μm, 236 μm, and 226 μm, respectively. The average widths of the coating wear marks under the magnetic field are significantly reduced compared with those without the magnetic field, and the

width of the coating wear marks decreases with the increase in magnetic field intensity. The width is narrowest at 12 T, which is 34.3% less than that without the magnetic field.

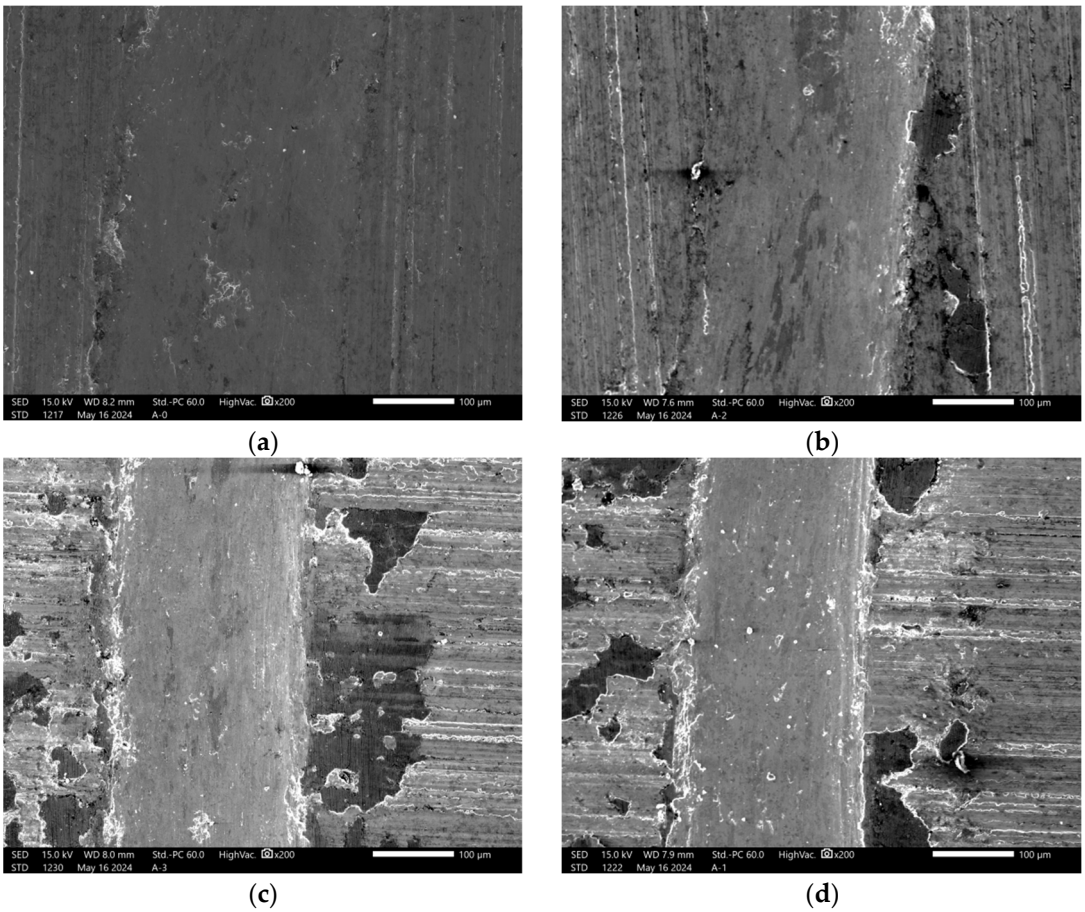

Figure 7. Wear mark widths of the cladding layer under different stable magnetic field intensities: (**a**) 0 T; (**b**) 4 T; (**c**) 8 T; (**d**) 12 T.

In order to further reveal the wear mechanism of the nickel-based cladding layer, the wear surface of the cladding layer with the highest hardness was analyzed by point scanning. Figure 8 shows the wear surface topography of the cladding layer at 8 T. As shown in the figure, there were many spalling areas and obvious grooves and adhesives on the wear surface. During the wear process, the plastic deformation of the cladding layer is obvious because the hardness is lower than the Si_3N_4 grinding ball, which results in the formation of a long strip of spalling area on the surface. With the progress of wear, part of the stripped material will be extruded to form new wear fragments, resulting in wear particle wear, and part of the stripped material will adhere to the cladding layer and the grinding ball, resulting in adhesive wear, which further aggravates the surface wear of the cladding layer [30]. At the same time, according to the EDS point-scanning results in Table 4, it can be seen that both the spalling area and the adhesion area contain oxygen elements. Combined with the generation of an oxide layer, it can be inferred that the cladding layer has oxidative wear. Therefore, it can be inferred that the wear mechanisms of the cladding layer are abrasive wear, adhesive wear, and oxidation wear [31].

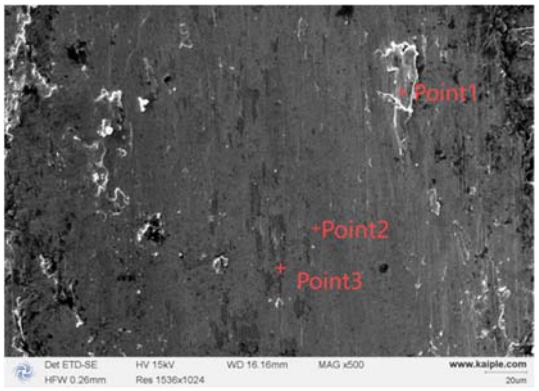

Figure 8. Wear surface morphology and EDS point-scanning area of the cladding layer at 8 T.

Table 4. Results of EDS point on the wear surface of the cladding layer.

Element (wt.%)	Point		
	1	2	3
C	20.00	17.01	12.16
O	5.38	0.07	17.04
Si	3.10	2.52	3.77
Cr	9.33	16.11	15.32
Fe	11.46	12.89	10.49
Ni	50.72	49.41	41.23

Figure 9 shows the three-dimensional macroscopic morphology of the nickel-based coating wear surface under different magnetic field intensities. It can be seen in the figure that the wear marks are roughly circular arcs with a high side and low middle, which is a typical shape formed by steel ball intrusion samples. As can be seen in Figure 9a, the marks are relatively smooth, which is because the coating is relatively uniform at 0 T, and the resistance to the grinding ball in the process of friction and wear is relatively small, so it presents a symmetrical arc in the depth direction. In the wear process, γ--Ni and hard phase CrB in the middle–upper parts of the coating have higher hardness and bonding strength, which protects part of the coating from being cut by friction pairs. This further explains the reason for the decrease in the wear of nickel-based coating assisted by the magnetic field.

The wear volume, ΔV, and wear rate, ω, of the nickel-based coating assisted by different magnetic field intensities are shown in Figure 10. The wear rate (ω) can be calculated by formula (1) [13]:

$$\omega = \Delta V / Pt \quad (1)$$

where ΔV (mm^3) represents the wear volume, P (N) represents the load, and t (s) represents the wear time.

With the increase in magnetic field intensity, the wear volume gradually decreases, and the wear volume of the coating at 12 T decreases by 81.13% compared with that at 0 T, which indicates that the wear resistance of the coating is further improved with the addition of magnetic field assistance, and the wear resistance is also improved with the increase in magnetic field intensity.

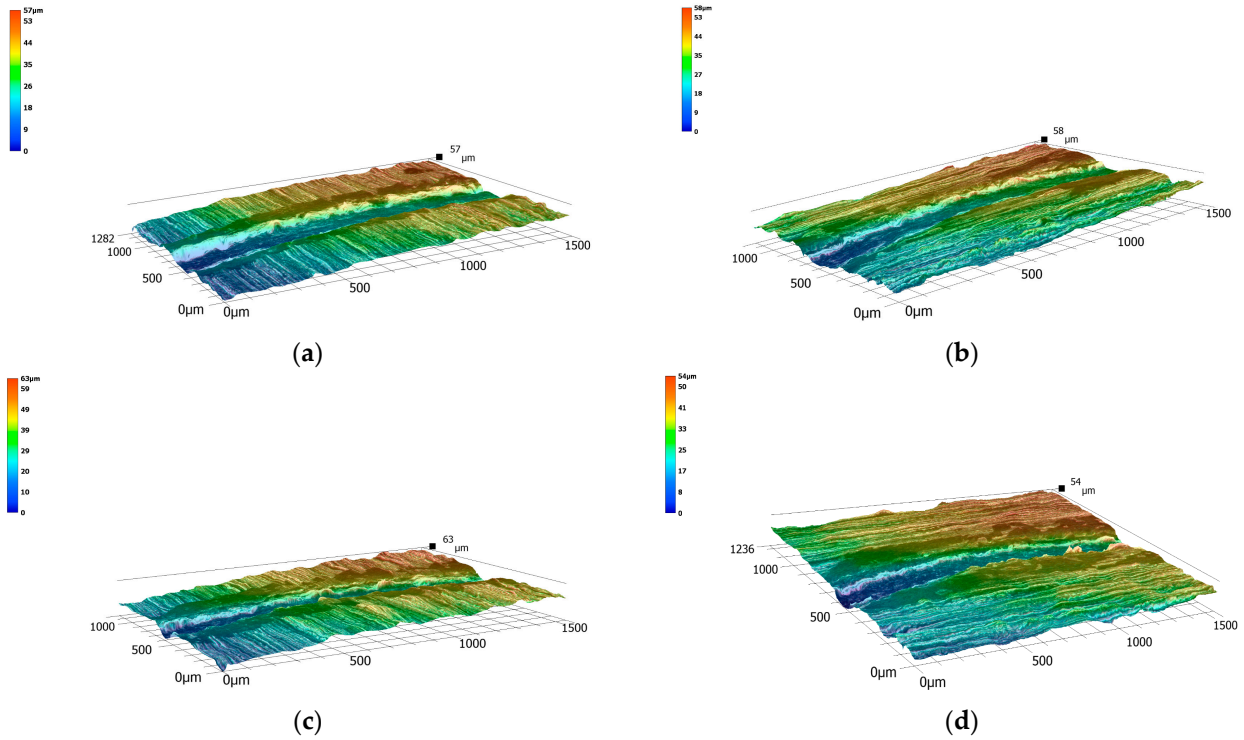

Figure 9. Wear 3D morphologies of the cladding layer under different stable magnetic field intensities: (**a**) 0 T; (**b**) 4 T; (**c**) 8 T; (**d**) 12 T.

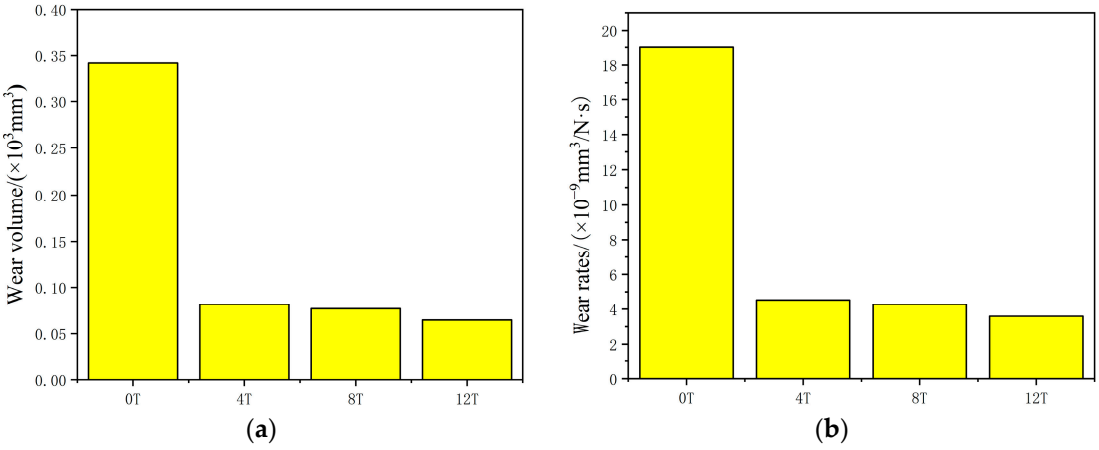

Figure 10. Parameters of wear under different stable magnetic field intensities: (**a**) wear volume; (**b**) wear rate.

3.6. Effect of an Electromagnetic Intensity on Corrosion Resistance

Figure 11 shows the potentiodynamic polarization curve of the cladding layer under four magnetic field intensities, and the corresponding electrochemical corrosion parameters are shown in Table 5. Among them, the more positive the corrosion potential (Ecorr), the smaller the corrosion current density (Icorr), which means the better the corrosion resistance of the coating [32]. Generally, the corrosion current density is the main parameter to judge the corrosion resistance. It can be seen from the figure that the coatings show similar curve trends under different stable magnetic field intensities. The corrosion potentials of the coatings with different stable magnetic field intensities are −0.655 V, −0.617 V, −0.498 V, and −0.597 V, respectively. With the increase in magnetic field intensity, the corrosion current density decreases gradually from 3.527×10^{-6} A·cm^{-2} at 0 T to 1.985×10^{-6} A·cm^{-2} at 8 T, a decrease of nearly half, reaching 43.7%. It shows that the

corrosion resistance of the coating increases with the increase in magnetic field intensity in a certain range.

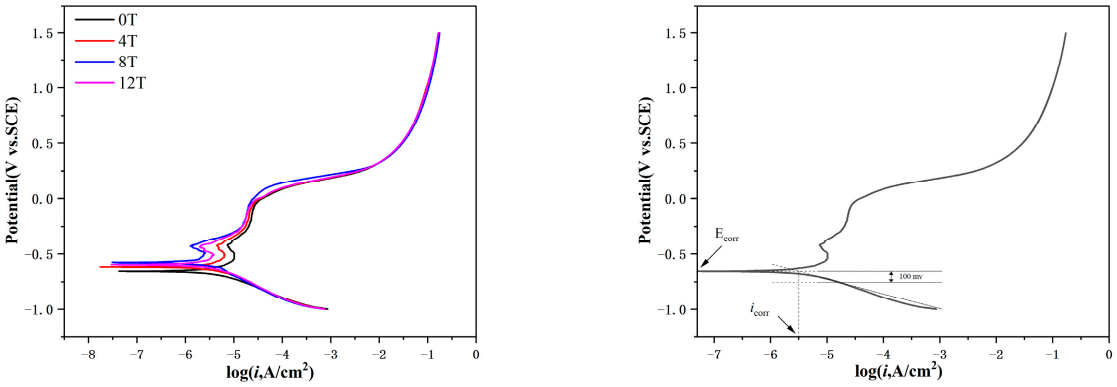

(**a**) (**b**)

Figure 11. (**a**) Potentiodynamic polarization curve under different stable magnetic field intensities; (**b**) illustration of corrosion current density determination by Tafel plot.

Table 5. Electrochemical corrosion parameters under different stable magnetic field intensities.

Magnetic Field Intensity	Icorr/(A·cm^{-2})	Ecorr/V	β_c/(V/decade)
0 T	3.527×10^{-6}	−0.655	−0.13569
4 T	3.059×10^{-6}	−0.617	−0.14888
8 T	1.985×10^{-6}	−0.498	−0.29783
12 T	2.362×10^{-6}	−0.597	−0.13841

In order to further verify the influence of different magnetic fields on the corrosion resistance of the nickel-based coating, electrochemical impedance spectroscopy (EIS) analysis was conducted, and an equivalent circuit model, R(QR), was established, as shown in Figure 12d. Where R_s represents the corrosion solution resistance between the two electrodes, CPE represents the constant phase element used to replace the capacitor, and R_{ct} represents the charge transfer resistance. Figure 12a shows the Nyquist curves of the coatings prepared under different stable magnetic field intensities, which are roughly parabolic in shape. The radius of the capacitor arc in the parabola indicates the degree of corrosion reaction between the cladding layer and the electrolyte interface. The larger the radius, the larger the impedance and the better the corrosion resistance. It can be seen from the figure that the cladding layer shows a larger capacitive arc radius under high magnetic field intensity, which means better corrosion resistance. Figure 12b is the mode value diagram of the coatings with different stable magnetic field intensities, and Figure 12c is the phase angle diagram of the coatings prepared with different stable magnetic field intensities. Generally speaking, the larger the impedance modulus, |Z|, and the larger the phase angle, the better the corrosion resistance of the material [33]. The osmotic resistance of the material is represented by the amplitude of the phase angle in the figure. Therefore, a higher phase angle indicates that the coating has better corrosion resistance. As can be seen in the figure, the curve impedance modulus |Z| and curve phase angle value of the sample prepared under a low-frequency band and high magnetic field intensity are higher, which indicates that there is a denser passivation film at the corrosion interface, and it has better corrosion resistance. Figure 12d shows the equivalent circuit fitted to the EIS data of samples at four magnetic field intensities. The EIS fitting results are shown in Table 6. The constant phase element (CPE) is used to replace the capacitive element, n is the exponential term in the constant phase angle element, the resistance of 3.5wt %NaCl solution between the working electrode and the reference electrode is represented by Rs, Rct represents the

charge transfer resistance, and $\sum\chi 2$ is the fitting error. It can be seen from Table 6 that the Rct of the sample at high magnetic field intensity is larger than that at low magnetic field intensity, indicating that the addition of a magnetic field can enhance corrosion resistance.

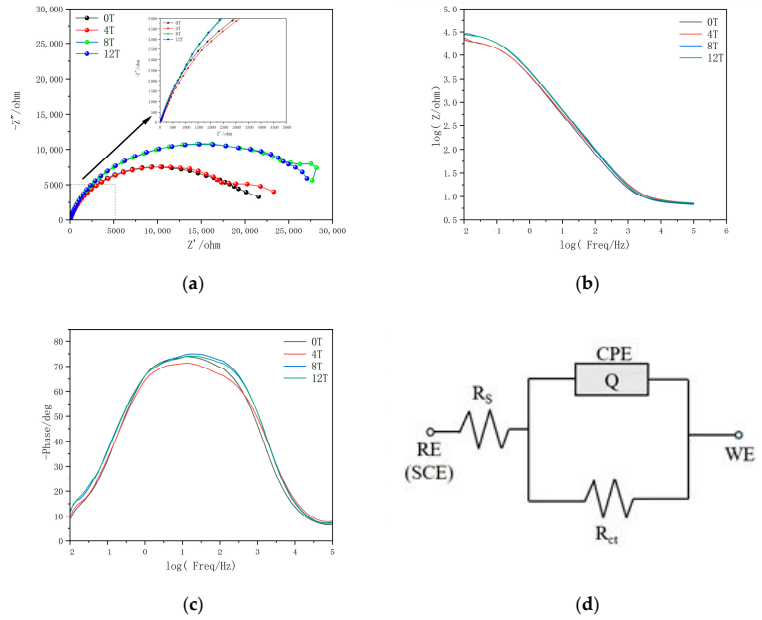

Figure 12. Impedance spectra under different stable magnetic field intensities: (**a**) Nyquist diagram; (**b**) mode diagram; (**c**) phase angle diagram; (**d**) equivalent circuit.

Table 6. EIS fitting results under different stable magnetic field intensities.

Magnetic Field Intensity	R_s ($\Omega \cdot cm^2$)	CPE ($\Omega^{-1} \cdot s^n \cdot cm^{-2}$)	n	R_{ct} ($\Omega \cdot cm^2$)	$\sum\chi^2$
0T	7.303	5.507×10^{-5}	0.841	2.113×10^{3}	1.818×10^{-3}
4T	7.383	5.71×10^{-4}	0.8084	2.306×10^{4}	1.716×10^{-3}
8T	6.884	4.648×10^{-5}	0.8395	2.738×10^{4}	3.481×10^{-3}
12T	7.313	4.422×10^{-4}	0.8373	3.254×10^{4}	2.429×10^{-3}

This may be due to the uneven distribution of phases and elements in samples without electromagnetic assistance, which will aggravate corrosion and greatly reduce the corrosion resistance of the material. The introduction of a magnetic field will not only make uniform the distribution of elements in the nickel-based coating but also increase the number of grains, thus increasing the grain boundary. Generally speaking, the corrosion is generally carried out along the grain boundary [34]. Grain boundaries represent corrosion channels, and the increase in corrosion channels will reduce the corrosion resistance of the cladding layer. However, the magnetic field-assisted suppression of element segregation in the cladding layer improves the uniformity of elements and reduces the number of local micro-galvanic cells [35]. At this time, due to the increase in grain boundaries, the growth of the passivation film accelerates, which hinders the progress of the anode reaction, and the overall corrosion current density decreases. At the same time, after the addition of the magnetic field, the matrix phase γ-Ni and hard phase CrB have high bond strength [36]. The uniform structure and element distribution improve the permeability resistance of the electrolyte, making it difficult for corrosive liquid to penetrate the structure, and ultimately improve its corrosion resistance [37,38]. This is consistent with the results of the phase angle and wear resistance test. Corrosion can be clearly defined as eight different types: uniform, galvanic, erosion, intergranular, dealloying, crevice, environmentally induced cracking,

and pitting corrosion [39,40]. According to the corrosion process, it can be concluded that the sample mainly experienced intergranular and galvanic corrosion.

4. Conclusions

In this paper, the macroscopic morphology, phase composition, microstructure, microhardness, wear resistance, and corrosion resistance of laser cladding nickel-based coating on Q345R steel with the assistance of different magnetic field intensities are mainly analyzed. The main results are as follows:

(1) With the increase in magnetic field intensity, the bonding strength of the cladding layer increases, and the width increases gradually from 4.02 mm at 0 T to 4.25 mm at 12 T. The crack phenomenon decreases gradually, and the dilution rate increases.

(2) Magnetic field-assisted laser cladding will not change the phase composition of the cladding layer, but the position of the diffraction peak will shift to lower angles due to the different degrees of lattice distortion. With the increase in magnetic field intensity, some of the microstructure of the coating is refined, and the hard phase CrB tends to form clusters.

(3) The microhardness of the coating with magnetic field assistance increases compared with that without magnetic field assistance and reaches the maximum at 8 T, which is 944 $HV_{0.5}$. The microhardness at 12 T does not increase but decreases and is lower than the other three coatings.

(4) With the assistance of the magnetic field, the COF of the coating decreases with the magnetic field intensity. The average COF of the coating at 12 T is 0.29, which is 6.5% lower than that at 0 T. With the increase in magnetic field intensity, the wear width, wear volume, and wear rate of the coating gradually decrease. The wear volume decreases by 81.13% at 12 T compared with that at 0 T.

(5) The current corrosion density of the coating decreases with the increase in the magnetic field intensity, and the corrosion potential reaches its maximum at 8 T. At low frequency and high magnetic field intensity, the coating has larger amplitude modulus and phase angle, indicating the enhancement of its corrosion resistance.

Author Contributions: Conceptualization, K.W. and Z.Z.; methodology, D.Z. and K.W.; validation, Z.Z.; formal analysis, D.Z. and D.J.; investigation, M.Z., J.Z. and H.H.; resources, Y.T. and Z.Z.; data curation, D.Z. and D.J.; writing—original draft preparation, D.Z., D.J.; writing—review and editing, Y.T., M.Z. and K.W.; supervision, K.W. and Z.Z.; project administration, K.W. and Y.T.; funding acquisition, K.W., H.H. and J.Z. All authors have read and agreed to the published version of the manuscript.

Funding: The authors would like to acknowledge the financial support for this work from the National Natural Science Foundation of China (52205334, 52075049), the Natural Science Foundation of Hunan Province (2022JJ40495), and the Sichuan Science and Technology Program(2024NSFSC0151).

Data Availability Statement: The original contributions presented in the study are included in the article, further inquiries can be directed to the corresponding authors.

Conflicts of Interest: The authors declare no conflicts of interest.

References

1. Price, S.; Figueira, R. Corrosion Protection Systems and Fatigue Corrosion in Offshore Wind Structures: Current Status and Future Perspectives. *Coatings* **2017**, *7*, 25. [CrossRef]
2. Mou, J.; Jia, X.; Chen, P.; Chen, L. Research on Operation Safety of Offshore Wind Farms. *J. Mar. Sci. Eng.* **2021**, *9*, 881. [CrossRef]
3. Xiang, D.; Liu, Y.; Yu, T.; Wang, D.; Leng, X.; Wang, K.; Liu, L.; Pan, J.; Yao, S.; Chen, Z. Review on wear resistance of laser cladding high-entropy alloy coatings. *J. Mater. Res. Technol.* **2024**, *28*, 911–934. [CrossRef]
4. Momber, A.W. Quantitative performance assessment of corrosion protection systems for offshore wind power transmission platforms. *Renew. Energy* **2016**, *94*, 314–327. [CrossRef]
5. Farayibi, P.K.; Abioye, T.E.; Clare, A.T. A parametric study on laser cladding of Ti-6Al-4V wire and WC/W2C powder. *Int. J. Adv. Manuf. Technol.* **2016**, *87*, 3349–3358. [CrossRef]

6. Sui, S.; Chew, Y.; Hao, Z.; Weng, F.; Tan, C.; Du, Z.; Bi, G. Effect of cyclic heat treatment on microstructure and mechanical properties of laser aided additive manufacturing Ti–6Al–2Sn–4Zr–2Mo alloy. *Adv. Powder Mater.* **2022**, *1*, 100002. [CrossRef]
7. Arias-González, F.; Del Val, J.; Comesaña, R.; Penide, J.; Lusquiños, F.; Quintero, F.; Riveiro, A.; Boutinguiza, M.; Pou, J. Fiber laser cladding of nickel-based alloy on cast iron. *Appl. Surf. Sci.* **2016**, *374*, 197–205. [CrossRef]
8. Zhu, L.; Xue, P.; Lan, Q.; Meng, G.; Ren, Y.; Yang, Z.; Xu, P.; Liu, Z. Recent research and development status of laser cladding: A review. *Opt. Laser Technol.* **2021**, *138*, 106915. [CrossRef]
9. Zhai, L.L.; Ban, C.Y.; Zhang, J.W. Investigation on laser cladding Ni-base coating assisted by electromagnetic field. *Opt. Laser Technol.* **2019**, *114*, 81–88. [CrossRef]
10. Wang, Z.; Zhou, H.; Chen, Z.; Zhu, Y.; He, F.; Xiang, N.; Wang, Y. Study on the effect of electromagnetic field on the segregation and structural property of Ni60 cladding layer. *Optik* **2023**, *272*, 170279. [CrossRef]
11. Wang, Q.; Zhai, L.L.; Zhang, L.; Zhang, J.W.; Ban, C.Y. Effect of steady magnetic field on microstructure and properties of laser cladding Ni-based alloy coating. *J. Mater. Res. Technol.* **2022**, *17*, 2145–2157. [CrossRef]
12. Zhang, X.; Cui, H.; Wang, J.; Zhang, G.; Zhao, Y.; Sun, K. Effects of TiB2+TiC content on microstructure and wear resistance of Ni55-based composite coatings produced by plasma cladding. *Trans. Nonferrous Met. Soc.* **2019**, *29*, 132–142. [CrossRef]
13. Wang, K.; Liu, W.; Du, D.; Chang, B.; Liu, G.; Hu, Y.; Tong, Y.; Zhang, M.; Zhang, J.; Ju, J. Microstructure and properties of K648 superalloy additively manufactured by extreme high-speed laser metal deposition. *Trans. Nonferrous Met. Soc.* **2024**, *34*, 2192–2203. [CrossRef]
14. Zhao, J.; Han, B.; Cui, G.; Zhang, S.; Li, M.; Wang, Y. Preparation of Ni55 + FeS composite coatings and their antifriction performances in artificial seawater. *Mater. Des.* **2017**, *131*, 375–383. [CrossRef]
15. You, W.; Wei, G.; Yinkai, X.; Huaixue, L.; Caiyou, Z.; Ming, X.; Hongqiang, Z. In-situ monitoring plume, spattering behavior and revealing their relationship with melt flow in laser powder bed fusion of nickel-based superalloy. *J. Mater. Sci. Technol.* **2024**, *177*, 44–58.
16. Zhang, Y.; Guo, W.; Shi, J.; Chi, J.; Chen, G.; Han, G.; Zhang, H. Improved rotating bending fatigue performance of laser directed energy deposited Ti6Al4V alloys by laser shock peening. *J. Alloys Compd.* **2024**, *980*, 173664. [CrossRef]
17. Lei, J.; Liu, G.; Li, H.; Han, H.; Di, R.; Lei, J. Gaussian and circular oscillating laser directed energy deposition of WC/NiCu composites. *Mater. Charact.* **2023**, *204*, 113218. [CrossRef]
18. WEI, W.; ZHENG, X.; CHEN, X.; ZHAI, Y.; CHENG, Q.; GUO, F.; HE, Q.; SU, W.; ZHANG, C.; RAN, H.; et al. Anisotropy of mechanical properties response on crystallographic features of GH5188 superalloy fabricated by laser powder bed fusion. *J. Adv. Manuf. Sci. Technol.* **2023**, *3*, 2023015. [CrossRef]
19. Wang, X.; Zhang, C.H.; Cui, X.; Zhang, S.; Chen, J.; Zhang, J.B. Microstructure and mechanical behavior of additive manufactured Cr–Ni–V low alloy steel in different heat treatment. *Vacuum* **2020**, *175*, 109216. [CrossRef]
20. Balyan, M.K. X-ray Bragg diffraction with allowance for the second derivatives of amplitudes in dynamical diffraction equations. *J. Contemp. Phys.* **2014**, *49*, 180–187. [CrossRef]
21. Lin, Y.; Yuan, Y.; Wang, L.; Hu, Y.; Zhang, Q.; Yao, J. Effect of electromagnetic composite field on microstructure and cracks of Ni60 alloy during solidification. *Acta Metall. Sin.* **2018**, *54*, 1442–1450. [CrossRef]
22. Kota, S.; Wang, W.; Lu, J.; Natu, V.; Opagiste, C.; Ying, G.; Hultman, L.; May, S.J.; Barsoum, M.W. Magnetic properties of Cr2AlB2, Cr3AlB4, and CrB powders. *J. Alloys Compd.* **2018**, *767*, 474–482. [CrossRef]
23. Wang, C.; Gao, Y.; Zeng, Z.; Fu, Y. Effect of rare-earth on friction and wear properties of laser cladding Ni-based coatings on 6063Al. *J. Alloys Compd.* **2017**, *727*, 278–285. [CrossRef]
24. Savrai, R.A.; Makarov, A.V.; Soboleva, N.N.; Malygina, I.Y.; Osintseva, A.L. The Behavior of Gas Powder Laser Clad NiCrBSi Coatings Under Contact Loading. *J. Mater. Eng. Perform.* **2016**, *25*, 1068–1075. [CrossRef]
25. Yao, G.; Yuan, J.; Pan, S.; Guan, Z.; Cao, C.; Li, X. Casting In-Situ Cu/CrBx Composites via Aluminum-Assisted Reduction. *Procedia Manuf.* **2020**, *48*, 320–324. [CrossRef]
26. Yao, G.; Cao, C.; Pan, S.; Yuan, J.; De Rosa, I.; Li, X. Thermally stable ultrafine grained copper induced by CrB/CrB2 microparticles with surface nanofeatures via regular casting. *J. Mater. Sci. Technol.* **2020**, *58*, 55–62. [CrossRef]
27. Wang, K.; Liu, W.; Li, X.; Tong, Y.; Hu, Y.; Hu, H.; Chang, B.; Ju, J. Effect of hot isostatic pressing on microstructure and properties of high chromium K648 superalloy manufacturing by extreme high-speed laser metal deposition. *J. Mater. Res. Technol.* **2024**, *28*, 3951–3959. [CrossRef]
28. Chiang, K.A.; Chen, Y.C. Microstructural characterization and microscopy analysis of laser cladding Stellite12 and tungsten carbide. *J. Mater. Process. Technol.* **2007**, *182*, 297–302. [CrossRef]
29. Morshed-Behbahani, K.; Farhat, Z.; Nasiri, A. Effect of Surface Nanocrystallization on Wear Behavior of Steels: A Review. *Materials* **2024**, *17*, 1618. [CrossRef]
30. Yutao, L.; Kaiming, W.; Hanguang, F.; Xingye, G.; Jian, L. Microstructure and wear resistance of in-situ TiC reinforced AlCoCrFeNi-based coatings by laser cladding. *Appl. Surf. Sci.* **2022**, *585*, 152703.
31. Jian, G.; Jiang, J.; Rui, W.; Jingjing, L.; Hongyao, Y.; Kaiming, W. Effects of Laser Scanning Rate and Ti Content on Wear of Novel Fe-Cr-B-Al-Ti Coating Prepared via Laser Cladding. *J. Therm. Spray Technol.* **2022**, *31*, 2609–2620.
32. Dai, X.; Xie, M.; Zhou, S.; Wang, C.; Gu, M.; Yang, J.; Li, Z. Formation mechanism and improved properties of Cu95Fe5 homogeneous immiscible composite coating by the combination of mechanical alloying and laser cladding. *J. Alloys Compd.* **2018**, *740*, 194–202. [CrossRef]

33. Lu, F.; Ma, K.; Li, C.; Li, C. Enhanced Corrosion Resistance of a Double Ceramic Composite Coating Deposited by a Novel Method on Magnesium-Lithium Alloy (LA43M) Substrates. *J. Therm. Spray Technol.* **2021**, *30*, 680–693. [CrossRef]
34. Li, W.; Xia, Y.; Fang, Y.; Song, H.; Lei, J. Effects of circular beam oscillation on microstructure, mechanical and electrochemical corrosion properties of laser melting deposited Inconel 625. *J. Manuf. Process.* **2022**, *84*, 847–858. [CrossRef]
35. Ji, X.; Wang, H.; Pang, X.; Zhang, H.; Chen, T.; Hu, Y.; Wang, K.; Zhang, J.; Zhang, X.; Tong, Y. Multinary intermetallic with enhanced catalytic activity and prolonged stability at high current density for electrochemical hydrogen production. *J. Alloys Compd.* **2024**, *976*, 173119. [CrossRef]
36. Di, J.; Zhi, C.H.; Jie, S.X.; Juan, L.X.; Feng, Z.X.; Hao, C.; Liang, M.G. Wear and corrosion resistance of CoCrNi composite coatings by laser cladding. *China Foundry* **2022**, *19*, 535–543.
37. Xu, X.; Du, J.L.; Luo, K.Y.; Peng, M.X.; Xing, F.; Wu, L.J.; Lu, J.Z. Microstructural features and corrosion behavior of Fe-based coatings prepared by an integrated process of extreme high-speed laser additive manufacturing. *Surf. Coat. Technol.* **2021**, *422*, 127500. [CrossRef]
38. Ralston, K.D.; Birbilis, N.; Davies, C.H.J. Revealing the relationship between grain size and corrosion rate of metals. *Scr. Mater.* **2010**, *63*, 1201–1204. [CrossRef]
39. Morshed-Behbahani, K.; Zakerin, N. A review on the role of surface nanocrystallization in corrosion of stainless steel. *J. Mater. Res. Technol.* **2022**, *19*, 1120–1147. [CrossRef]
40. Morshed-Behbahani, K.; Nasiri, A. Corrosion response of steels fabricated through arc directed energy deposition additive manufacturing: A review. *Mater. Horiz.* **2024**, *11*, 3011–3037. [CrossRef]